A GCM Simulation of the Climate 6000 Years Ago

NICHOLAS M. J. HALL AND PAUL J. VALDES

Department of Meteorology, University of Reading, Reading, United Kingdom

(Manuscript received 9 August 1994, in final form 28 November 1995)

ABSTRACT

Two 10-yr integrations of the UGAMP GCM are presented. Each has a full seasonal cycle, T42 resolution, interactive land and sea ice, and prescribed sea surface temperatures. They differ in that one integration represents present day climate (PD) and the other has a perturbed orbit and reduced atmospheric concentrations of CO_2 appropriate to the climate of 6000 years ago (6 kyr, hereafter 6k). The 6k integration produces enhanced continental warmth during summer and cold during winter. Changes in atmospheric temperature gradients brought about by the surface response lead to altered jet stream structures and transient eddy activity, which in turn affect precipitation patterns. Tropical ''monsoon''-type circulation patterns are also affected, also leading to altered precipitation. Many of the changes in hydrology mimic the geological record remarkably well: the Sahel is much wetter, as are the midwestern United States and the Mediterranean regions; California and northern Europe are drier. Processes leading to the model's surface responses in both temperature and hydrology are described in detail. Finally, the sensitivity of the results to an alternative, objective definition of the 6k calendar is investigated. This sensitivity is found to be smaller than the overall signal to the extent that the principal conclusions are not altered.

1. Introduction

The climate of 6000 years ago represents a good test bed for evaluating GCM performance for a number of reasons. First, it is a relatively recent paleoclimate and consequently relatively data rich. Proxy data are available from pollen records (Bartlein and Webb 1985; Huntley and Prentice 1988) and lake levels (Street-Perrott and Harrison 1985) and can be used for model validation (see also Wright et al. 1993). Second, compared to other paleoclimates, it is possible to model the climate of 6000 years ago with relatively simple changes to model boundary conditions. Observational evidence from ocean sediment cores (Ruddiman and Mix 1993; Morley and Dworetzky 1993) indicates that changes in sea surface temperature are modest, so in fact it is only the radiative forcing that is altered in the experiment presented here. Finally, a further motivation for modeling this specific period with the boundary conditions described below is that at a later date it will be possible to compare these model results with those from other GCMs as part of a standardized set of experiments under the auspices of the Paleoclimate Model Intercomparison Project (PMIP).

Previous GCM studies of the mid-Holocene have been carried out by Kutzbach and Guetter (1986, hereafter referred to as KG), Liao et al. (1994, hereafter LSM), Kutzbach and Gallimore (1988), Gallimore and Kutzbach (1989), and Mitchell et al. (1988). Of these, the first two papers include results of GCM integrations for 6000 years ago, and the rest concentrate on 9000 years ago, but they also have some relevance here. The radiative forcing anomaly for both these periods acts to amplify the seasonal cycle in the Northern Hemisphere and attenuate it in the Southern Hemisphere. The analysis of these experiments has mainly been in terms of the response of the land masses (chiefly the Northern Hemisphere continents) to the change in the seasonal cycle of radiation and the associated changes in surface temperature, atmospheric circulation, and hydrology. Comparisons of GCM results with various types of paleoclimatic data have also been made, principally in the Cooperative Holocene Mapping Project (COHMAP Members 1988), but see also Kutzbach and Street-Perrott (1985) and LSM.

In their perpetual August run, KG report temperatures 2°–4°C higher than for the present day at midlatitudes in Asia and North America, with an associated lowering of sea level pressure and large-scale low-level convergence in these areas. This in turn affects the vertical velocity in the midtroposphere. The hydrological cycle is modified so that generally speaking both precipitation and evaporation are increased over midlatitude continents, but evaporation increases more than precipitation, leading to drier conditions at the surface. The subtropics, on the other hand, become significantly wetter, particularly in the Sahel region as the low-latitude summer monsoon circulations intensify, bringing stronger south-

Corresponding author address: Dr. Nicholas M. Hall, CIRES, University of Colorado, Campus Box 449, Boulder, CO 80309-0449.

erly onshore winds to West Africa, India, and the Gulf of Mexico. Conversely, in the perpetual January case, KG's simulations have generally shown weaker Southern Hemisphere monsoon circulations with reduced precipitation over Southern Hemisphere land masses. These results are typical of the mid-Holocene simulations referred to above.

Some similarity should be expected between these GCMs and the one presented here as far as the simple thermal response of the continents is concerned. To this extent, the results should also resemble those derived from two-dimensional energy balance models. However, factors such as atmospheric circulation or cloud radiative effects, which are more GCM specific, will lead to differences. The GCM used by LSM, for example, has an interactive ''slab'' ocean that can allow for enhanced warming in high northern latitudes. One point worthy of note is that in common with some other GCMs within PMIP, the GCM presented here is of higher resolution than in previous studies and therefore can potentially represent entities such as midlatitude depressions, and their effect on the general circulation more accurately.

In this paper we present results from two full seasonal cycle integrations of the UGAMP (U.K. Universities Global Atmospheric Modelling Programme) GCM. One representing the present day climate (PD) and one intended to simulate the climate of 6000 years before present (k kyr BP, hereafter 6k). The two integrations differ only in the seasonal cycle of insolation at the top of the atmosphere and in the concentration of atmospheric carbon dioxide.

In section 2, the GCM is described and the different boundary conditions used for the two integrations shown. Then in section 3 the results for the surface response of the GCM to these different boundary conditions are presented, and the corresponding change in the atmospheric circulation and precipitation is described. In section 4 a brief comparison is made with the geological data available from pollen and lake level records. Section 5 then contains further analysis of the causes of the temperature anomalies presented in section 3 in terms of physical diagnostics. Finally, some difficulty arises in the timing of the seasons for the purpose of defining averaging periods that are appropriate for comparison between the PD and 6k runs. This is discussed briefly in section 6, and the sensitivity of the results to two different definitions of the seasons is ascertained. Section 7 contains a summary and conclusions.

2. The model and boundary conditions

The UGAMP GCM is based on the forecast model of the European Centre for Medium-Range Weather Forecasting (ECMWF). The version we are using is nearly identical to that currently being used in the Atmospheric Model Intercomparison Experiment (AMIP), which is described in detail by Slingo et al. (1994).

It is a spectral model, using a triangular truncation at total wavenumber 42. The physical parameterizations are evaluated on a longitude–latitude grid of 128 × 64 points. The model has 19 levels in the vertical, five of which are within 150 mb of the surface.

TABLE 1. Orbital parameters for the two integrations. Details in text.

	Present day (PD)	6000 years ago (6 kyr BP)
Eccentricity, e	0.016724	0.018682
Obliquity, ϵ	23.446^0	24.105^0
Perihelion date, ω	282.04	180.87

The model includes the following physical parameterizations. The radiation scheme is that of Morcrette (1990) and includes a predictive cloud scheme based on relative humidity criteria (Slingo 1987). The gravity wave drag scheme of Palmer et al. (1986) is used. The vertical advection uses a total variance diminishing scheme (Thuburn 1993). An important modification included in this version of the model is that the convection scheme is based on the work of Betts and Miller (1986).

Surface albedo and roughness length are prescribed, but land-surface temperature and soil moisture content are calculated using a three-layer diffusive soil model. There is a no-flux boundary condition at the bottom of the soil model (approximately 6 m thick). This is essential for paleoclimate simulations because it allows the surface temperature to respond fully to forcing rather than being tied to some current climatology on long timescales. The model sea surface temperatures are prescribed and are the same in both PD and 6k runs, a reasonable assumption for the mid-Holocene, and are based on the data set of Alexander and Mobley (1976).

The sea ice edge is prescribed as the -2°C contour in the sea surface temperature. On the sea ice itself, the surface temperature is calculated using a simple thermodynamic sea ice model in which heat is stored by and diffused vertically across a slab of ice 2 m thick. Over sea ice the albedo is set to 0.55. Snow cover is represented as a layer of variable depth that sits on top of the soil layer. The thickness of the layer is simply determined from the balance between accumulation and ablation, without compacting. The albedo increases with snow depth, up to a maximum value of 0.8.

The atmospheric concentration of carbon dioxide is set at 345 ppmv for PD and to the preindustrial value of 280 ppmv for 6k (see Watson et al. 1990).

The insolation at the top of the atmosphere is prescribed as a function of latitude, longitude, time of day, and time of year. It is different in the two runs and is calculated according to three orbital parameters, which have been determined using the method prescribed by Berger (1978). These parameters are the eccentricity of the earth's orbit, e, the obliquity or tilt of the earth's axis of rotation, ϵ (as measured from a line perpendicular to the ecliptic plane), and the date on which the perihelion occurs, ω (measured in solar days from the

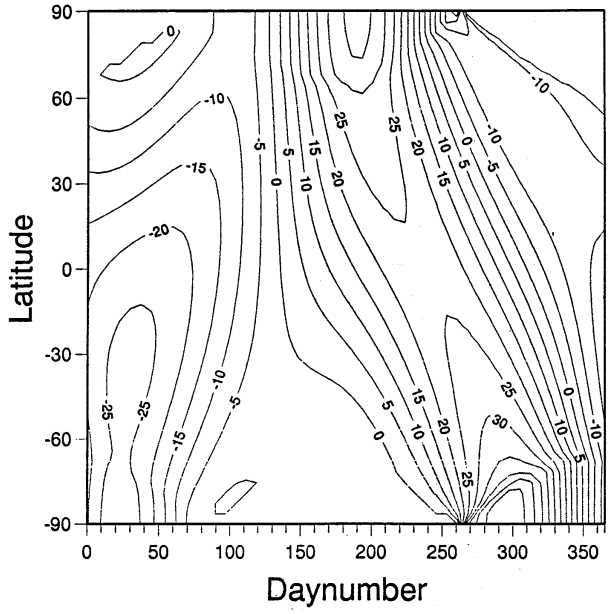

FIG. 1. The difference (6k–PD) in top of the atmosphere incoming solar radiation in watts per square meter as a function of latitude and time of year.

vernal equinox). The values used for these parameters are given in Table 1 for the two integrations. The model runs with a 365-day year and the four seasons are defined as 90-day periods that are centered on the usual triplets of months: MAM, JJA, SON, and DJF (more details are given in section 6). However, the lengths of time between the cardinal astronomical points (solstices and equinoxes) differ between PD and 6k, leaving an arbitrary choice as to where the calendar months should fall relative to, say, the vernal equinox. The convention adopted here is that the vernal equinox occurs at 1200 UTC 21 March in both PD and 6k runs. The consequences of this assumption are examined in section 6.

Figure 1 shows the anomaly in incoming radiation at the top of the atmosphere (6k–PD). For PD, the perihelion occurs close to the winter solstice, reducing seasonality in the Northern Hemisphere. For 6k, however, the perihelion occurs near the autumnal equinox. This, combined with a greater axial tilt, leads to an enhancement of seasonality in the Northern Hemisphere with a particularly rapid transition from spring to summer. The anomaly plot shows the perturbation to the radiative forcing due to the altered orbit and should be borne in mind throughout what follows. It should, of course, also be remembered that CO_2 levels are reduced for the 6k run.

It is worthwhile at this point listing the principal differences between this experiment and other work. This model differs from that of KG by having higher reso-

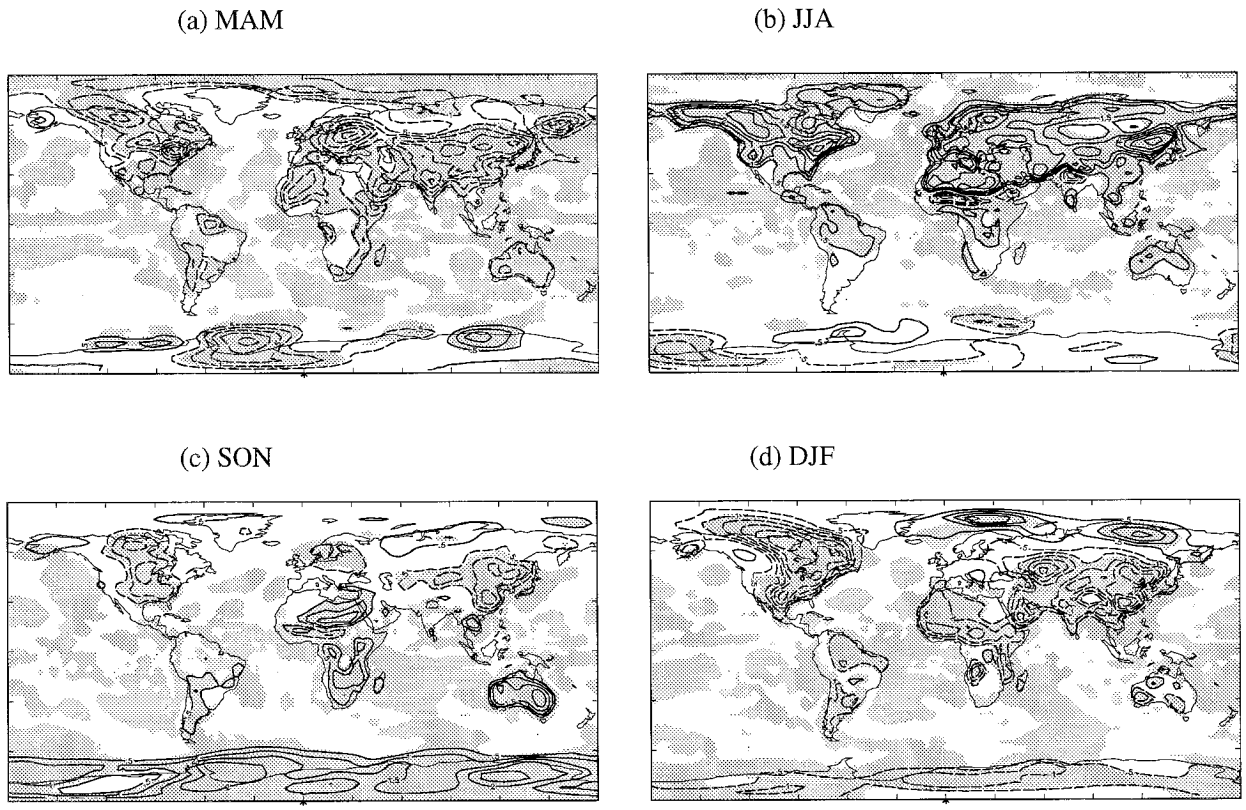

FIG. 2. Surface air temperature anomaly (6k–PD) for (a) MAM, (b) JJA, (c) SON, and (d) DJF. Contour interval is 0.5°C. The zero contour has been omitted for clarity. Negative contours are dashed. Areas where the signal is significant at the 95% confidence level have been shaded.

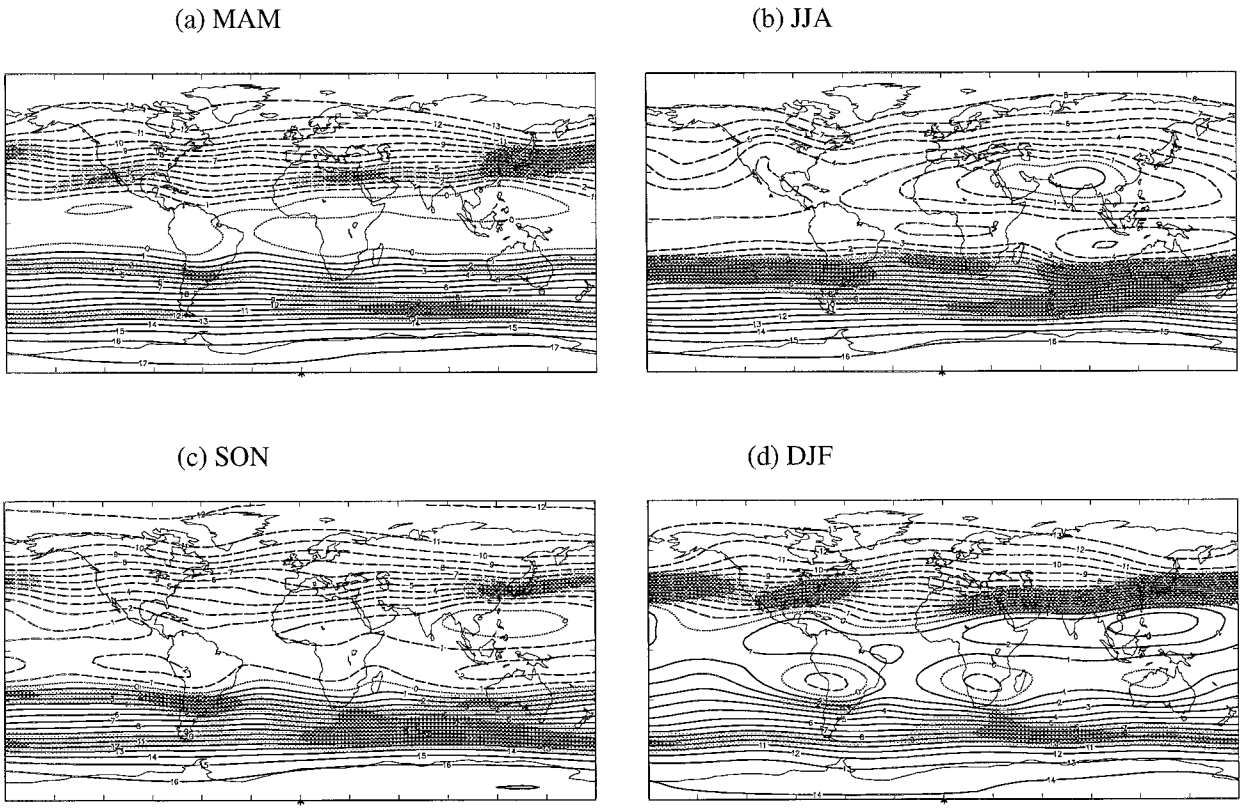

FIG. 3. (a)–(d) Contours of 200-mb streamfunction and 200-mb isotachs for PD. Contours every 10^7 m^2 s^{-2}. Zero contour dotted. Negative contours dashed. Wind speeds greater than 30 m s^{-1} shaded. Wind speeds greater than 35 m s^{-1} shaded heavily. (e)–(h) Anomaly (6k–PD) in streamfunction (contours every 2×10^6 m^2 s^{-2}), Zero contour omitted. Negative contours dashed. Areas where the wind speed has changed by more than 3 m s^{-1} shaded.

lution; reduced carbon dioxide at 6k; a full seasonal cycle; a sea ice model; and an interactive soil model that includes soil moisture calculations. This model differs from that of LSM only in the first two of these points. The model used by LSM has two different cloud schemes and includes a simple calculation of sea surface temperatures based on prescribed horizontal heat fluxes and oceanic heat capacity. This model and that of KG use sea surface temperatures prescribed from present day observations.

In a 10-yr GCM integration it is always possible that the ''signal'' observed, and described as a response to changing forcing or boundary conditions, may be smaller than the natural variability of the system, especially in regions where the variability is large. The statistical significance of the results that follow has been assessed through *t* tests, the results of which are shown for some of the fields considered. Attention is only drawn to features that are significant at a confidence level of 95% or more.

3. The atmospheric response

a. Surface air temperature

It can be seen from Fig. 1, that the anomaly in the top of the atmosphere incoming radiation primarily represents a perturbation to the seasonal cycle. In MAM there is a negative anomaly in the Northern Hemisphere but a rapid transition to a positive anomaly in JJA. This positive anomaly then sweeps down to the Southern Hemisphere in SON and rapidly changes sign leaving a strong negative anomaly in the Southern Hemisphere in DJF. For the 6k climate we should therefore expect the major land masses of the Northern Hemisphere to be cooler in MAM but warmer in JJA. We should also expect the land masses of the Southern Hemisphere to be warmer in SON but cooler in DJF.

In what follows, things will be generally described season by season, with individual paragraphs clearly labeled to aid the reader.

1) MAM

Figure 2 shows the 10-yr mean surface air temperature anomaly (6k–PD) for the four seasons. In MAM the Northern Hemisphere land masses are indeed cooler. This is also the season with the largest cold anomalies over the North Pole. North America and northern Asia are colder by up to 2°C and eastern Europe is 3°C colder at 6k. There is also a 2°C cold spot in the Weddel Sea.

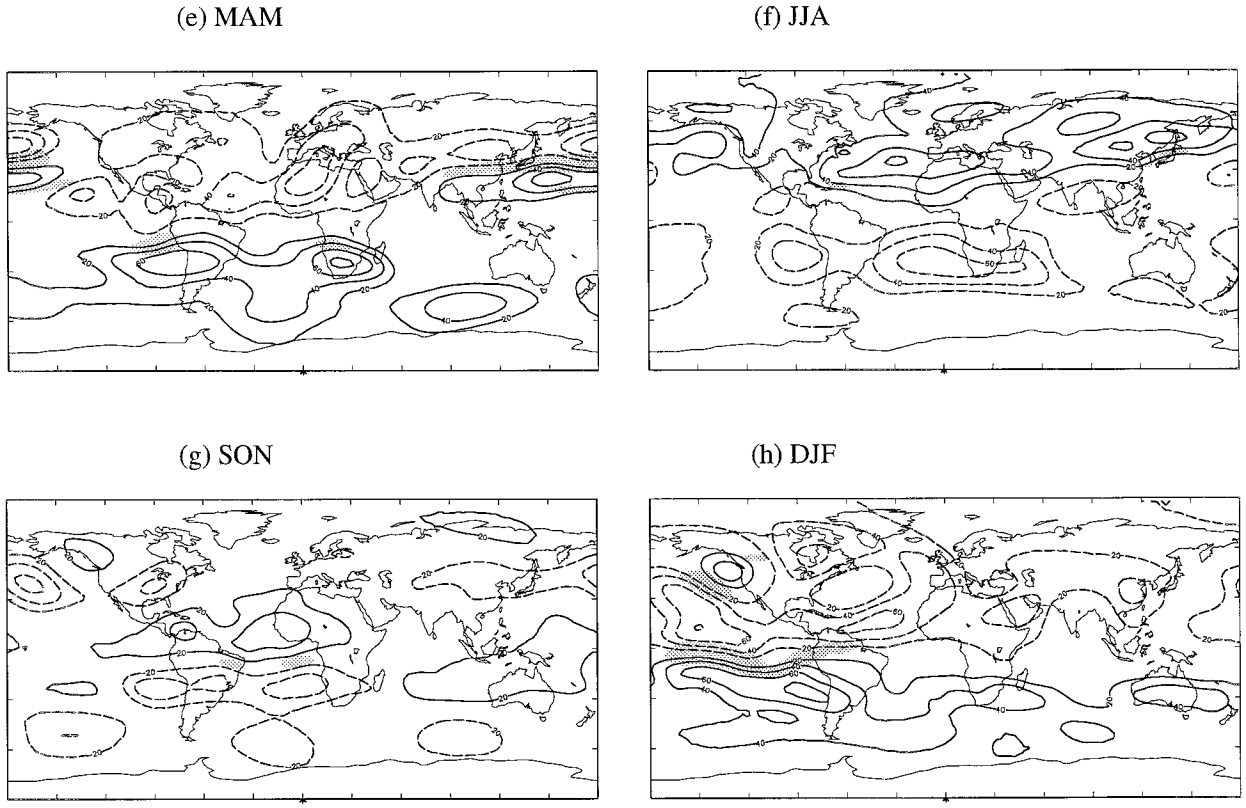

FIG. 3. Continued.

2) JJA

By JJA, the fast transition from a colder spring to a warmer summer is in evidence, especially in the Northern Hemisphere. North America, North Africa, Europe, and parts of Asia are 2°C warmer, but the warming is more patchy over northern Siberia. There are no large anomalies in the Southern Hemisphere for JJA.

3) SON

In SON, the positive radiation anomaly has migrated to the Southern Hemisphere and it can be seen that Antarctica is warmer by more than 2°C in places. Parts of the Northern Hemisphere continents have started to cool. North America and northeastern Asia are over 1°C cooler. However, North Africa and northern Siberia have remained warm.

4) DJF

The arctic warming in the Eastern Hemisphere persists into DJF and actually increases to 3°C in two small regions. Apart from this, the land is generally colder at 6k in DJF, especially in northeastern North America. Antarctica has switched from being warmer to being colder in DJF, as expected from the rapid change in the Southern Hemisphere incoming radiation anomaly.

b. The time mean circulation

The atmospheric response to these surface temperature anomalies has often been described in terms of the large-scale low-level divergence field. The simple (thermally direct) large-scale response to a warm anomaly is a drop in the sea level pressure accompanied by cyclonic and convergent (subgeostrophic) anomaly in the surface wind. Conversely, cooling will be associated with a raised sea level pressure and an anticyclonic and divergent surface wind anomaly. This view of the large-scale circulation seems to provide an approximate description of the changes in the sea level pressure and surface wind. However, there are instances where the geostrophic component of the response in the surface wind dominates, with important consequences. Changes in the midtropospheric temperature gradients are also implicated in altered midlatitude jet structures and transient behavior. All these aspects of the atmospheric circulation can play an important role in altering precipitation patterns, which are ultimately verifiable against geological data. Changes in upper tropospheric circulation are depicted in Fig. 3, which shows the streamfunction and jet maxima at 200 mb for PD (Figs. 3a to 3d) and the anomaly, 6k–PD, (Figs. 3e to 3h).

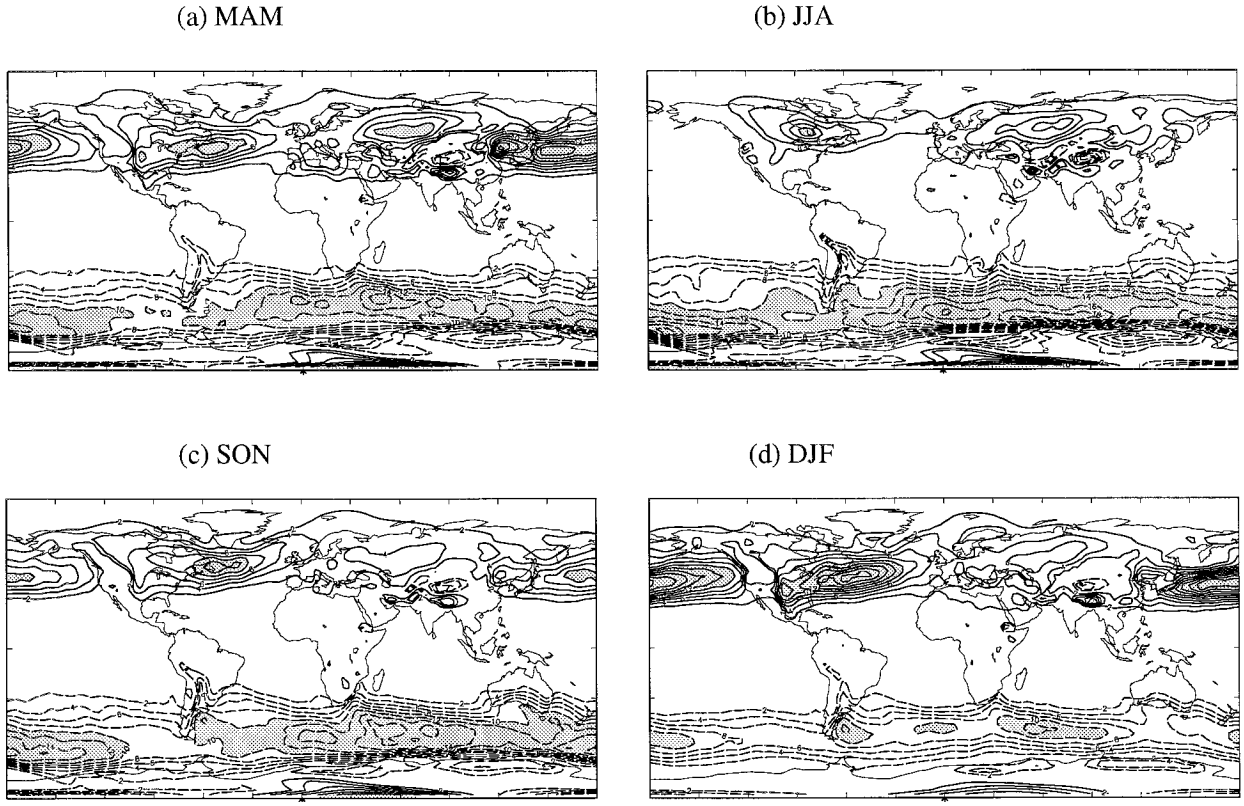

FIG. 4. 850-mb high-pass filtered transient eddy meridional temperature flux. (a)–(d) PD. Contours every 2 K m s^{-1}. Zero contour omitted. Negative contours dashed. Values greater than 10 K m s^{-1} or less than -10 K m s^{-1} shaded. (e)–(h) Anomaly (6k–PD). Contours every 1 K m s^{-1}. Zero contour omitted. Negative contours dashed. Areas where the signal is significant at the 95% confidence level have been shaded.

1) MAM

The cold Northern Hemisphere continents in MAM have a raised sea level pressure by up to 3 mb in central Asia, whereas over the sea the pressure is lowered, particularly in the North Pacific where there is a negative anomaly of 4 mb. The associated increase in cyclonic low-level circulation implies enhanced westerlies in the northern Pacific. This is a deep feature. The midtropospheric westerlies are also enhanced in the northern Pacific, by up to 8 m s^{-1}, as seen in Fig. 3e, which shows a dipole in 200-mb streamfunction anomaly. This change is consistent with the increased baroclinicity associated with the deep cooling over Asia (up to 2°C at 500 mb) that spreads out into the North Pacific. The anomalous cyclonic circulation seen in Fig. 3e shows a deep ''cold core'' structure. In contrast to this, the cold anomalies over North America and eastern Europe, where the static stability is higher by a factor of more than two, are relatively shallow features.

2) JJA

As the Northern Hemisphere continents become warmer at 6k in JJA, so the pressure anomaly drops and becomes negative over central Asia, the Mediterranean region, and Greenland. The summer monsoon is slightly enhanced at the surface, with onshore winds increased by up to 1 m s^{-1} in the Arabian Sea, and to a lesser extent in the Gulf of Mexico, but the most striking change in the low-level circulation in the summer is seen over the Sahel region, where a strong (2.5 m s^{-1}) southwesterly anomaly develops in the surface wind, a large part of which is ageostrophic. Northeasterly anomalies of similar magnitude also exist in Central America and in the Philippines. At upper levels the onset of the Asian monsoon is well illustrated by the arrival of an anticyclone over Tibet and the associated reversal of the upper-level winds over India, as seen in Fig. 3b. This large-scale manifestation of the upper-level monsoon is almost completely unchanged at 6k. The zero contour in the anomaly plot goes through the center of the anticyclone (Fig. 3f). This result is surprising in the light of previous simulations of the climate of 9000 years ago. KG and Mitchell et al. (1988) both report intensified Asian monsoons for that period and clearly associate this with the radiative forcing anomaly. It may be related to the difference in convection scheme, which is to some extent constrained by the prescribed sea surface temperature in this integration. The divergent component of the circulation does show some change. There

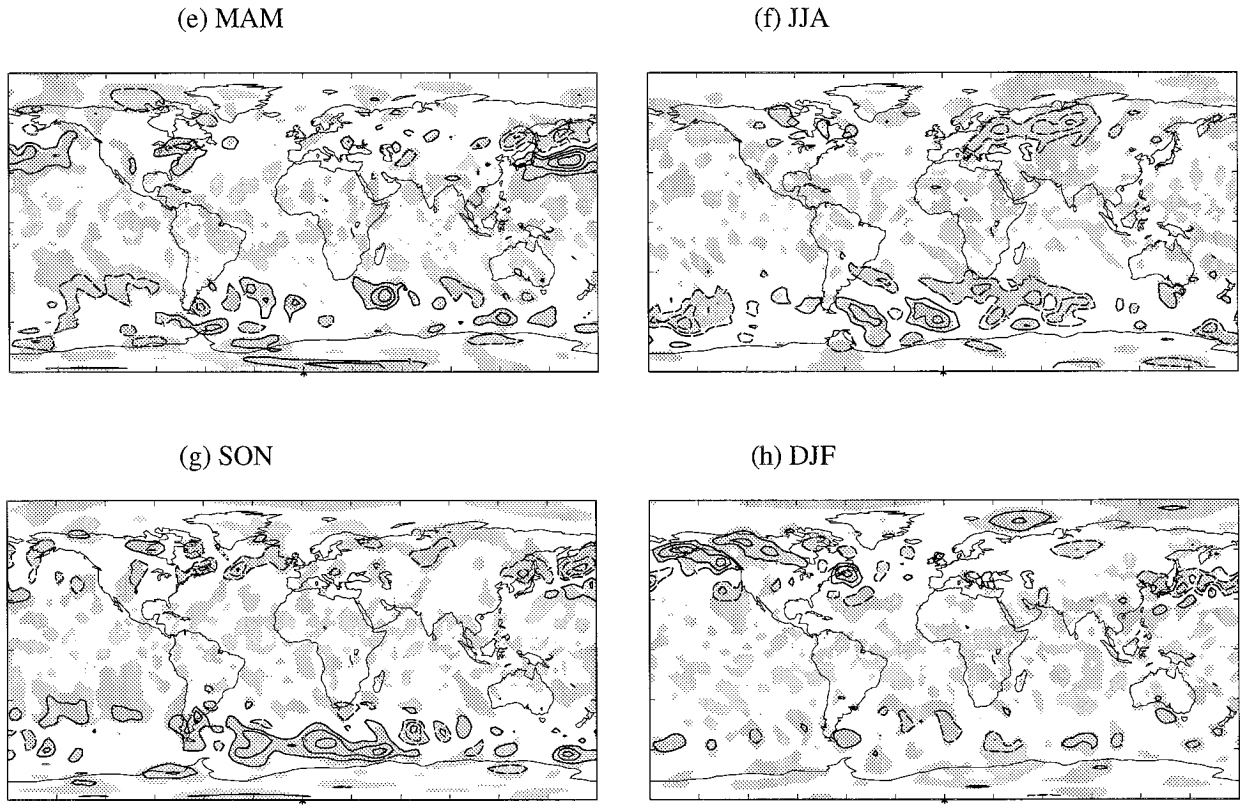

FIG. 4. Continued.

is an upward vertical velocity anomaly of 0.8 mb h^{-1} at 500 mb over Tibet, and a stronger divergent flow at 200 mb in this region (not shown).

3) SON

Most of the larger sea level pressure anomalies in SON simply represent minor perturbations to the strong Southern Hemisphere surface westerlies. The arctic warmth at 6k during SON extends up into the troposphere, and midtropospheric temperature gradients are slightly weakened at 6k. The strength of the midlatitude jets is not greatly altered.

4) DJF

The situation over Siberia becomes more complicated in DJF. The Arctic is warmer, but central Asia is colder, and there is generally higher pressure over land. The largest surface pressure anomaly in DJF is a high off the west coast of North America, which represents a significant westward shift of the Aleutian low. The geostrophic anomaly associated with this is a considerable weakening of the Pacific westerlies that impinge upon the coast of California during winter. The 2°C surface cold anomaly over eastern North America is still present at 500 mb. In addition there is a warm anomaly in the western North Atlantic located beneath the positive (anticyclonic) 200-mb streamfunction anomaly shown in Fig. 3h. This deep baroclinic structure, caused by the relatively cold land mass, accounts for the strengthening of the Atlantic jet and the weakening of the westerlies off the west coast of North America, also shown in Fig. 3h. However, the largest change in the zonal wind is an 8.5 m s^{-1} increase in the tropical westerlies in the eastern Pacific ''waveguide'' region. Indeed, there may be some connection between activity in this region and a possible wavelike response over North America that is apparent in the 200-mb streamfunction anomaly shown in Fig. 3h.

c. Midlatitude storm tracks

We have seen that the changed orbital configuration has led to changes in the seasonal cycle of temperature over land. This occurs both at the surface and aloft. We have also seen that differences in the horizontal temperature gradient in the midtroposphere brought on by different land–sea temperature contrasts have led to changes in the strength of the midlatitude jets. These seaboard temperature contrasts are also important for the formation and maintenance of the storm tracks (see Hoskins and Valdes 1990). The storm tracks are in turn responsible for a large proportion of the precipitation at midlatitudes. Midlatitude baroclinic systems grow at

a rate that is partly determined by the meridional temperature gradient. Maxima in the midtropospheric baroclinicity occur at midlatitudes on the western sides of the Northern Hemisphere oceans and at midlatitudes in the Southern Hemisphere, centered over the southern Indian Ocean.

From a consideration of changes in baroclinicity, one can attempt to interpret direct indications of transient activity. One such indicator is the transient eddy meridional temperature flux, which is displayed in Fig. 4, again for PD and the anomaly, 6k–PD. The fluxes are shown at the 850-mb level and are time filtered using the 3-day block filter introduced by Hoskins et al. (1989) and also described in Hall et al. (1994). Essentially it is a high pass filter with a cutoff at approximately 6 days, and therefore captures fluxes associated with developing midlatitude baroclinic systems.

Comparing the model results with the observations of Hoskins et al. (1989), based on 10 years of ECMWF analyses, the model does reasonably well in both positioning and intensity of the storm tracks in both hemispheres. The main deficiency of the model is that the high-pass transient eddies in the Northern Hemisphere are too weak during SON.

1) MAM

The increased seaboard temperature contrasts associated with the land cooling in MAM are clearly reflected in the increased meridional temperature flux for 6k, shown in Fig. 4e. There is a larger change in the North Pacific, where the maxima in the baroclinicity also intensify as expected, and shift southward, leading to the changes in the jet structure described above. This southward intensification is also clearly seen in the temperature flux. The relatively cool Southern Hemisphere land masses lead to a reduced temperature gradient in the Southern Hemisphere. Southern Hemisphere temperature fluxes are slightly weaker in general for 6k (with associated positive anomalies shown in Fig. 4e), particularly in the southern Atlantic and Indian Oceans.

2) JJA

During JJA the Northern Hemisphere storm tracks are weak and show no appreciable change at 6k, despite the dramatic swing toward weakened seaboard temperature contrasts. In the Southern Hemisphere, the storm track is at its strongest with a maximum in activity in the southern Indian Ocean. The general warming of land in JJA has led to increased meridional temperature gradients in the Southern Hemisphere and increased southward temperature fluxes in this region.

3) SON

The Northern Hemisphere storm tracks during SON are rather weaker than observations would suggest. They weaken further at 6k. Both storm track areas show negative anomalies in temperature flux.

4) DJF

Cold anomalies have set in in DJF, particularly over North America. The resulting increase in baroclinicity in the North Atlantic storm track region, associated with the enhanced jet described above, leads to increased temperature flux in this region. The Pacific storm track region shows a slight increase in baroclinicity, but it is not localized and does not appear to have a significant effect on the tropospheric transient eddy heat fluxes. However, in the northeastern Pacific along the south coast of Alaska, there is an area of greatly enhanced temperature gradients at 6k and an associated increase in transient eddy temperature flux.

d. Precipitation and evaporation

Apart from surface temperature, the other main area where comparison with paleoclimatic data is possible concerns land hydrology. This is very much an ''end product'' of a GCM and depends on many interconnected processes and parameterizations. In the GCM under consideration here there are two ways in which precipitation can be formed. The convection scheme referred to in section 2 is responsible for most of the tropical precipitation, whereas a large proportion of the precipitation at higher latitudes results from a simpler scheme that rains out any supersaturation due to large-scale ascent. This occurs in regions of large-scale low-level convergence and in developing baroclinic systems. All these mechanisms are of importance in assessing the difference in climate 6000 years ago, but the largest differences will be seen to be due to changes in deep convection.

Figure 5 shows the difference, 6k–PD, in average precipitation for each season. Even in the anomaly fields, one can see the march of the seasons, marked by the passage of the intertropical convergence zone (ITCZ), and the associated anomalies in convective rainfall between its northern extreme in JJA and its southern extreme in DJF.

1) MAM

Comparing PD with 6k during MAM, when the ITCZ lies over the Southern Hemisphere continents, it can be seen that South America and South Africa were drier at 6k in this season, except for a wet patch over northern Brazil, where the convective rainfall maximum has intensified. A negative anomaly exists over northern China due to diminished convective rainfall in colder conditions with weaker southeasterlies, but there is slightly more rainfall in the midwestern United States. Northern Europe is drier and the Mediterranean wetter. Finally, both large-scale and convective precipitation are enhanced in the intensified Pacific storm track, especially

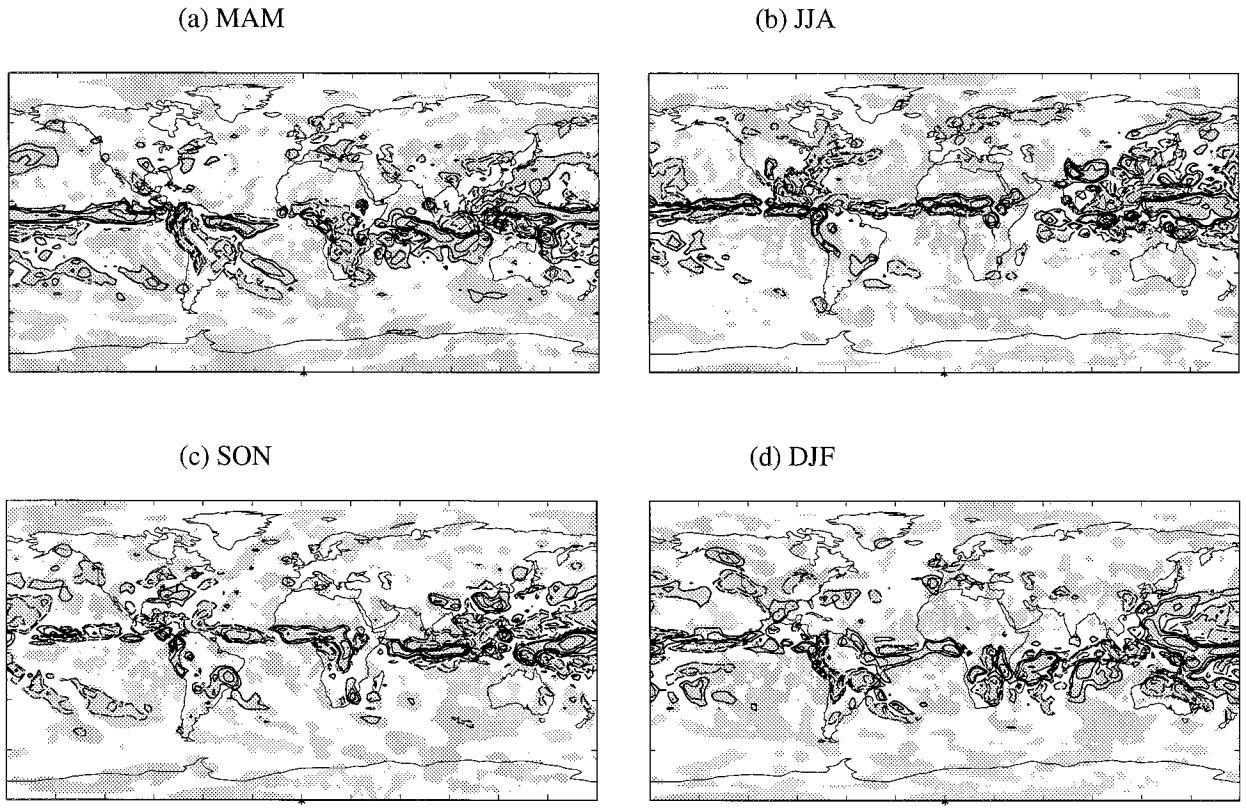

FIG. 5. Anomaly (6k–PD) in total precipitation in millimeters per day. Contours sequentially double, starting at 0.5, 1, 2, 4, etc. Zero contour omitted. Negative contours dashed. Areas where the signal is significnt at the 95% confidence level have been shaded.

in the region of increased ascent at the exit of the strengthened Pacific jet. This is also true to a lesser extent for the Atlantic storm track.

2) JJA

The dry anomaly in southern Africa has disappeared by JJA, but the Sahel region to the north is much wetter. This coincides with the region of large surface southwesterly anomalies. The monsoon rainfall over India is relatively unchanged at 6k. This is consistent with the lack of any intensification of the onshore surface wind on the subcontinent. There is, however, a slight positive precipitation anomaly to the east, where onshore southerlies are enhanced at 6k. There is also a very large positive anomaly over Tibet. Thus it could be argued that the first-order monsoon precipitation pattern in the model has intensified, although it is poorly represented on the subcontinent itself. The midwestern United States is also wetter during the warm JJA season. All these anomalies are associated with increased convection. Northern Europe is again slightly drier at 6k. Despite the increased Southern Hemisphere storm track activity during JJA, there is remarkably little to show in terms of increased precipitation and anomalies are generally small in the Southern Hemisphere during this season.

3) SON

In SON the ITCZ begins to move south again and the rains return to southern Africa. However, it is still mainly northern and western Africa that is anomalously wet at 6k. This could be due to a delay in the movement of the local ITCZ, driven by a hotter Sahara. The Indian monsoon has retreated but the rain belt in the Indian Ocean is enhanced at 6k, and the anomalous precipitation over Tibet persists. The high temperatures spreading to the Southern Hemisphere have not in general been accompanied by increased convective activity, with the exception of one isolated area in Brazil and one in South Africa. There is now an increase in the convective rainfall off the east coast of North America at 6k as the temperature has increased over the sea and decreased somewhat over the land.

4) DJF

In DJF the Southern Hemisphere continents have their maximum convective rainfall. However, the warm anomalies of SON are no longer present and the convection is weaker for 6k than for PD. Southern Africa, South America, and also Australia are all drier as a result of weaker convective activity. At high latitudes, in ad-

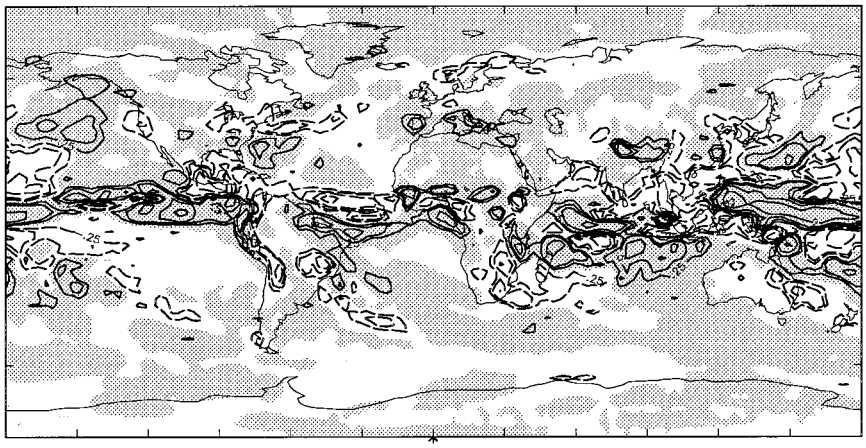

FIG. 6. (a) Anomaly (6k–PD) annual mean in $p - e$ (precipitation − evaporation) in millimeters per day. Contours follow doubling style of Fig. 5, starting at 0.25 mm day^{-1}. Negative contours dashed. Positive values shaded.

dition to changes in the divergent component of the circulation, changes in the geostrophic circulation come into play. California is much drier at 6k, but the west coast of Canada is wetter. This is consistent with changes in the jet structure and low-level circulation. It is also consistent with changes in transient activity shown in Fig. 4h. The westerlies on the California coast are reduced, but they are increased farther to the north. There are corresponding downward (1.6 mb h^{-1}) and upward (1.0 mb h^{-1}) anomalies in the 500-mb vertical velocity respectively. These changes in precipitation, at least over land, are mainly due to changes in the large-scale condensation in ascending air. Northern Europe is still drier, but over Spain there is increased precipitation, associated with increased surface westerlies coming from the Atlantic. The slight enhancement in the strength of the Atlantic storm track during this season associated with the increased land–sea temperature contrast off North America shows up as a positive anomaly in convective rain confined to the western Atlantic.

We have gone into considerable detail about how the seasonal cycle of precipitation has changed around the world. As mentioned above, precipitation is the end product of a large number of interconnected processes and it is important to see how any annual mean anomaly in the precipitation is composed and how this composition may vary from model to model since it is conceivable that different models may give a similar signal in the annual mean precipitation anomaly but for different reasons. However, the relevant climatic variable for comparison with most paleoclimatic data is the annual mean in some measure of surface wetness. Figure 6 shows the annual mean anomaly (6k–PD) in precipitation minus evaporation ($p - e$). Changes in $p - e$ are generally dominated by changes in precipitation in the Tropics, while in midlatitudes the precipitation and evaporation signals tend to cancel one another out, particularly over land. Many of the features already described for the individual seasons are prominent in the annual mean: the wet Sahel; dry southern Africa, South America and Australia; wet tropical eastern Pacific; wet Tibet; wet midwestern United States but a dry West Coast; and dry northern Europe but a wet Mediterranean.

4. Comparison with geological data

Validation data comes from a variety of sources and applies variously to specific seasons or annual mean quantities. It is principally surface temperature and some measure of surface moisture that is verifiable against geological evidence. We shall restrict ourselves to a brief verbal comparison of our results with the data studies in the literature, concentrating on the land surface on a region by region basis.

a. Eurasia

Huntley and Prentice (1988) have used pollen from mixed deciduous forests, which were more extensive at 6k, to reconstruct European July temperatures. They concluded that Europe was up to 2°C warmer during the 6k summer, the maximum occurring in northern and midcontinental Europe. Winters were colder in western and central Europe but warmer and with less snow cover in northern Europe. Farther to the east, data indicates warming over Russia (Klimanov 1984), which intensifies toward the north and east. The increased monsoon rains in northern Africa extended out to the Arabian peninsula, where lake levels were high (Roberts and Wright 1993). Data from a number of sources (Winkler and Wang 1993) indicate that China was generally wetter at 6k, with warmer summers and colder winters. Lake levels were high throughout China, except in the arid steppe region north of Tibet.

The model reproduces the European summer warm-

ing and places a maximum greater than 2°C in central and northern Europe during JJA in accord with the data. The maximum also diminishes as one heads east through northern Russia. During the winter season, the model does not produce a strong signal over Europe, but there is a cold spot during MAM over eastern-central Europe. The model does not appear to produce simultaneous warming of northern Europe with a cooler Mediterranean region during any season, and the only substantial change in precipitation is a wetter Iberian peninsula during DJF. However, the annual mean $p - e$ indicates a wetter Mediterranean and drier northern Europe. Arabia is wetter in the model at 6k, particularly in the southwest during summer. The accentuated seasonal cycle of temperature over China is picked up well by the model, but the pattern of $p - e$ is patchy. Eastern China and Tibet are much wetter, but central China is slightly drier in the model.

b. The Americas

At 6k prairies had expanded to their maximum extent in the American Midwest and the southern spruce border was at its northernmost extent (Bartlein and Webb 1985), indicating warmer summers at 6k throughout the continental interior. However, pollen data analyzed by Webb et al. (1993) indicate that northeastern Canada was cooler during July by up to 2°C, and the east coast of the United States and Florida were also slightly cooler. Arctic Canada, on the other hand, showed increased ice melt, indicating that this was an area of mid-Holocene summer warmth (Koerner and Fisher 1990). During January, Webb et al. (1993) also show from pollen data that Quebec and the Great Lakes region were up to 4°C warmer. Central-western Canada shows temperatures similar to present day (Ritchie and Harrison 1993) but was also drier at 6k, especially in the south. Data from lake levels imply that 6k was a time of maximum dryness on the eastern side of the continent but that the west coast of the United States was dry to the north and wet to the south at 6k. The 6k period was characterized by changing conditions in much of South America, and moisture patterns are complicated. Pollen data (Markgraf 1993) indicate dry conditions over the southern part of the continent, getting cooler to the south. Lake levels were relatively high in the north and on the Galapagos Islands.

The model simulates a warmer JJA, by more than 2°C in eastern and northwestern Canada, but there is little change in the southern and eastern United States. This appears to contradict the cool conditions inferred by Webb et al. (1993) over Labrador during July, although a cold spot does persist in the model during MAM in this location. During DJF there again appears to be a conflict between the model and the inferences of Webb et al. as the model shows cold anomalies centered on the eastern side of the continent. The contrast in wetness between California (drier) and the midwest (wetter) is well captured by the model. The simulated changes in hydrology over South America show considerable regional detail but can broadly be said to be consistent with observations. An area of increased precipitation exists in the north and out into the Pacific, while the Andes are generally drier.

c. Africa and Australasia

The most striking difference in surface moisture for the mid-Holocene is the increased wetness in northern Africa, as revealed by lake-level data (Street-Perrott and Harrison 1985; Street-Perrott and Perrott 1993). The increased wetness at 6k is concentrated in eastern equatorial regions (the Rift Valley), across the Sahel, and especially in the northwest (Atlas Mountains). Southern Africa is also slightly wetter at 6k. Analysis of lake-level and pollen data by Harrison and Dodson (1993) shows that southeastern Australia was much wetter at 6k. Evidence also exists that it was wetter in western Australia, but New Guinea was drier. New Zealand was wetter along its east coast (McGlone et al. 1993).

The model is very successful in reproducing the large increase in North African rainfall. However, in the model the increased wetness is too concentrated in the Sahel strip, and the large anomalies expected from the data in the regions of the Rift Valley and the Atlas Mountains do not appear. Southern Africa is actually drier in the model, although the data do not suggest this. The model contradicts all the observations for the Australian continent. There is a reduction in $p - e$ in Australia and New Zealand, and results from New Guinea are inconclusive.

5. Surface fluxes and heating rates

In this section we delve deeper into the causes of the temperature anomaly distributions presented at the beginning of section 3. Thus far these surface temperature anomalies have been used as a starting point for a discussion of the changes in atmospheric circulation, precipitation, and evaporation. However, the real starting point should be the anomaly in top of the atmosphere incoming radiation shown in Fig. 1. This anomaly gives rise to an altered balance of vertical fluxes at the surface. We will concentrate on the land surface in the following because due to the no-flux deep soil boundary condition, the land surface is allowed to find its own equilibrium temperature, and the surface fluxes over land must be in approximate balance.

1) MAM

The general lowering of Northern Hemisphere temperatures over land during MAM is concentrated in eastern Europe and northwestern North America rather than being evenly spread continent wide (see Fig. 2). These are shallow features and by 500 mb the cooling is most

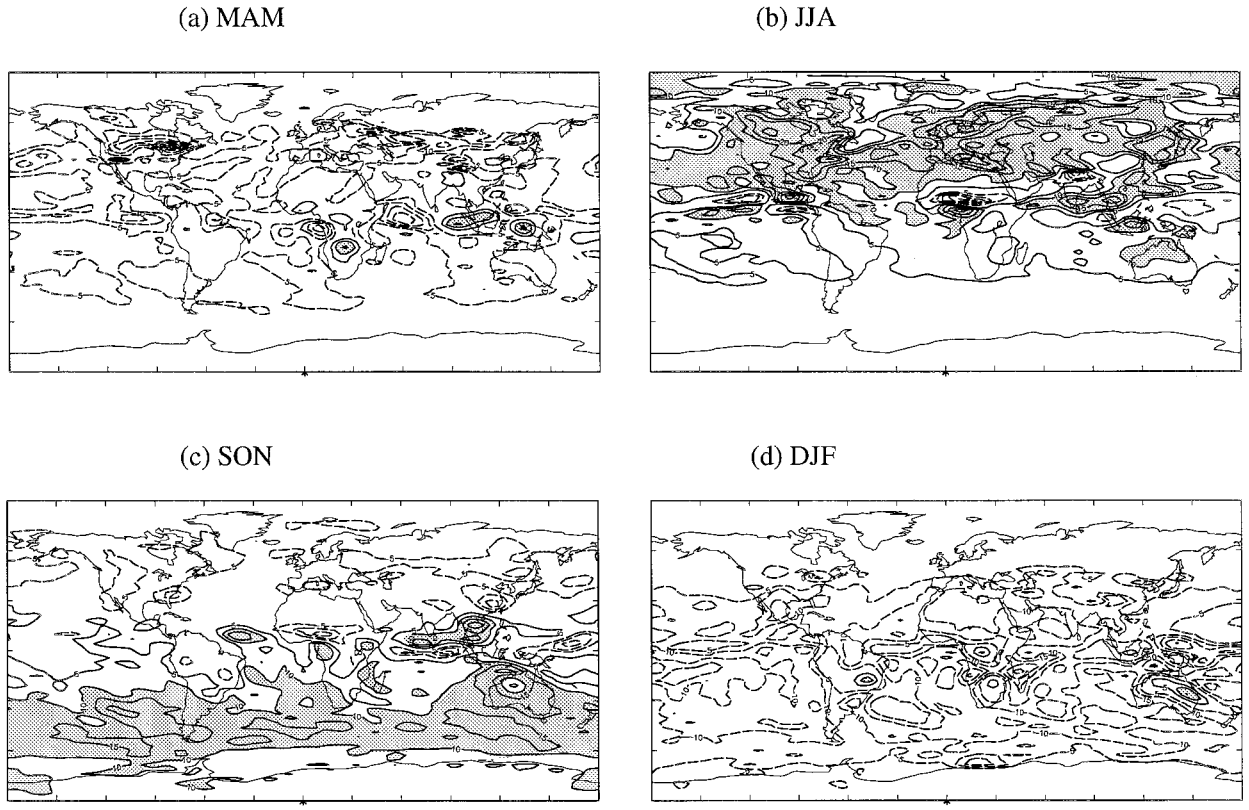

FIG. 7. Anomaly (6k–PD) in surface net solar radiation (positive downward). Contours every 5 W m^{-2}. Zero contour omitted. Negative contours dashed. Values greater than 10 W m^{-2} shaded.

intense over eastern Asia and in the North Pacific. However, it is of interest to discuss these local features in terms of the surface energy balance. Figure 7 shows the anomaly (6k–PD) in surface solar radiation for the four seasons. The maximum reduction in surface solar radiation over land, with negative values of more than 15 W m^{-2}, is concentrated into a narrow band in central Asia and North America. A compensating decrease in upward thermal radiation is also concentrated into this region together with reduced sensible heating to the atmosphere (not shown). The distribution of the downward solar radiation anomaly largely reflects a similar distribution at the top of the atmosphere. The sharp increase in cloudiness toward the pole in both PD and 6k runs reduces the incoming solar radiation to the extent that the effective anomaly is substantially reduced at higher latitudes. Changes in overall cloudiness with longitude are also consistent with the zonal structure of the solar radiation and the effective anomaly. The southern edge of snow cover also follows a similar path, and albedo effects associated with the migration of snow cover may serve to enhance the anomaly.

2) JJA

By JJA the Northern Hemisphere land masses have switched to being anomalously warm. This warming is concentrated in eastern Eurasia, northern Africa, and high latitudes in North America, but not northern Siberia. This contrast in the latitude of maximum warming between the two continents persists deep into the troposphere. The pattern of warming is again coincident with the form of the surface solar radiation anomaly as seen in Fig. 7b. One can make a connection between this asymmetry and actual changes in cloud cover. Total cloud cover is increased over Siberia but decreased over Europe by over 10% in a region of around 40% cloud cover. Associated with the increased convective precipitation in the Sahel strip during this season there is a significant increase in cloud cover, up to 20% in a region where the cloud cover is around 50%. This has the effect of reducing the surface solar radiation by up to 20 W m^{-2} in this locality, accounting for the cold anomalies seen in Fig. 2b.

3) SON

In SON the increased incoming solar radiation moves to the Southern Hemisphere and the southern continents are warmer for 6k than for PD. The response of the Southern Hemisphere is much as expected. The surface solar radiation is increased almost everywhere, and this effect is accentuated in regions of scant cloud cover, particularly Australia, where the surface solar radiation

is increased by up to 20 W m^{-2} and there is a corresponding increase in upward thermal radiation. At high latitudes in the Northern Hemisphere, where one might expect cooling in this season, some warm anomalies persist. The forcing anomaly is comparatively unimportant in these areas since cloud cover is everywhere greater than 70% and is almost total at the pole. North Africa is over 2°C warmer in this season. It is possible that this is a lagged response to the summer warming, as the deep soil layer is also anomalously warm having been heated over the summer.

4) DJF

Southern Hemisphere incoming solar radiation is strongly reduced during DJF and this is the season when Antarctica shows the most extensive cold anomalies. Negative anomalies exist in the surface solar radiation over most of the globe but there are a few isolated positive anomalies on the Southern Hemisphere continents, particularly Australia. These are associated with weak areas of warming and increased upward thermal radiation and are due to a reduction in cloud cover at 6k of up to 8% in areas where cloud cover is about 50%. In the Northern Hemisphere there is some asymmetry between the responses of the two major land masses to reduced solar radiation. North America is very cold, as is much of central Asia, but northern Siberia actually exhibits strong warm anomalies. There is no clue as to how this situation comes about from the vertical energy budget, but it is consistent with changes in the low-level circulation. Strong northwesterly anomalies exist in the region of the weak polar easterlies, bringing cold air over northern Canada, while the warm patch north of Scandinavia sits in an area of anomalous warm advection brought on by a strong southwesterly change to the surface winds. Eastern Siberia experiences a warming in the region of extreme minimum temperatures that may also be associated with westerly anomalies in an area of very weak prevailing wind.

6. Sensitivity to definition of calendar

The details of the earth's orbit for 6k and PD were laid out in section 2. It was also noted that an arbitrary choice was made in defining the position in this orbit that the conventional seasons occur at 6k. There is nothing unique about the choice of 21 March for the vernal equinox at 6k, and in principle any other day of the year could have been chosen. This issue has no bearing whatsoever on annual mean quantities, such as those shown in Fig. 6, but could obviously have great importance for the seasonal mean anomalies shown in most of the other figures. A possible alternative to choosing 1200 UTC 21 March is to choose a date for which the root-mean-square of the incoming solar radiation anomaly (6k–PD), weighted for area at a given latitude, is

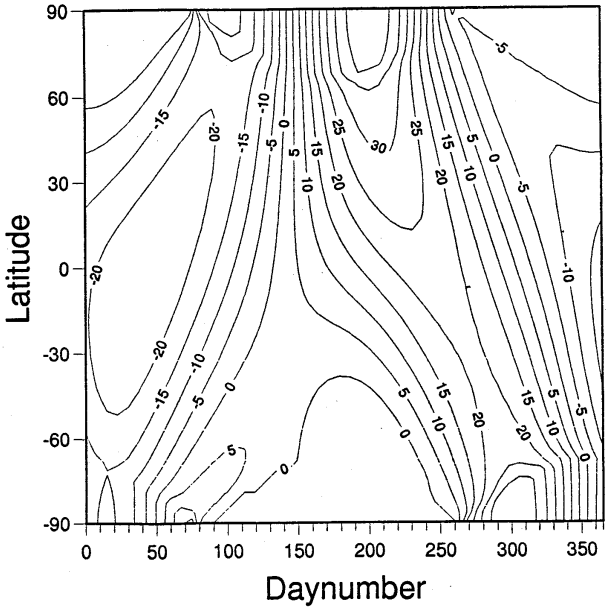

FIG. 8. Top of the atmosphere incoming solar radiation anomaly for shifted vernal equinox date (see text). Contours in watts per square meter as in Fig. 1.

minimized globally as a function of latitude and time of year. Thus the quantity

$$\int_0^{365} \int_{-90}^{90} (S_{6k} - S_{PD})^2 \cos^2\phi \, d\phi \, dt$$

is minimized, where S_{6k} and S_{PD} are the top of the atmosphere incoming solar radiation in watts per squared meter for 6k and PD, respectively, ϕ is latitude in degrees, and t time of year in days. This method is a variant of an original idea suggested by Taylor (1992, personal communication), and its numerical solution yields a vernal equinox date of 0712 UTC 24 March (2.30 days later). Figure 8 shows the new radiative forcing anomaly with this definition of the calendar at 6k (to be compared with Fig. 1). It can be seen that one of the effects of the minimization is actually to increase the contrast between MAM and JJA in the Northern Hemisphere. The large positive anomaly at high latitudes in the Southern Hemisphere during SON is, however, reduced.

In the model runs the data are stored every 0.75 days and the results are presented for seasons 90 days long, so that they can be time filtered in the same way for calculation of high-pass transients. The central point of each 90-day model season was made to coincide with the central point of its corresponding season in the 365-day calendar year. Then the 6k output was reanalyzed, shifting the model seasons 2.25 days backward in time relative to the orbit to coincide very closely with the optimum forcing shown in Fig. 8. New surface temperature anomalies were evaluated. The largest differences occur in MAM, and Fig. 9 shows the departure from the previous surface temperature anomaly (see Fig. 2a) for

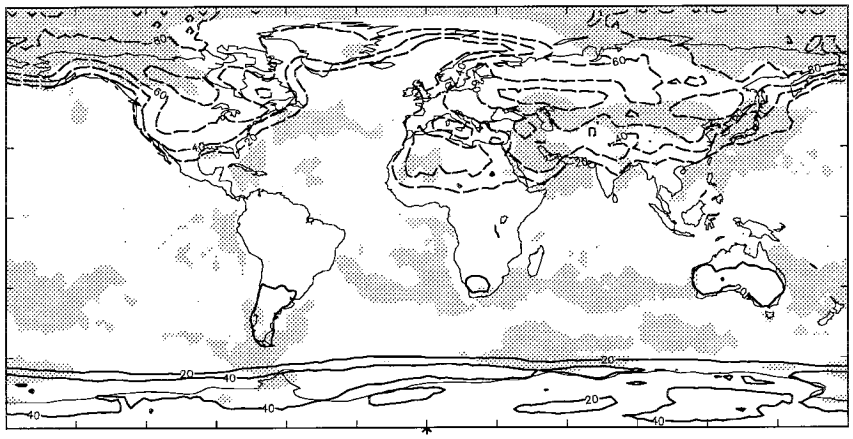

FIG. 9. Difference in surface air temperature for 6k run between having a shifted vernal equinox and not having it, that is, the anomaly (shift − no shift) for MAM. See text for details. Contours every 0.2°C. Zero contour omitted. Negative contours dashed. Areas where the signal is significant at the 95% confidence level have been shaded.

this season. It can be seen that the Northern Hemisphere cooling has been enhanced. This could be regarded as a rather perverse consequence of an attempt to minimize the anomaly! But it still serves as a measure of the sensitivity of the experiment to this type of adjustment. The maximum enhancement to the cooling is about 1°C and it is statistically significant in some regions, particularly central Asia and northern Canada. It represents a signal of about 30% of the climate signal, so for the type of adjustment chosen here, it could be viewed as important for MAM. However, it in no way affects any of the conclusions drawn in this paper, and for other seasons the effect is weaker and less significant.

7. Concluding remarks

The change in the earth's orbit at 6k is primarily a perturbation to the seasonal cycle. It provides for a particularly simple experiment with a GCM because the radiative forcing is the only boundary condition to be changed. We have described in depth the response of a GCM to this simple perturbation to the seasonal cycle and attempted to explain the chain of consequences of this altered boundary condition in a step by step manner, taking each season in turn and working from the most direct response to the most indirect. The complexity of the atmosphere and the GCM inevitably makes this task difficult. However, it is of fundamental importance since the more indirect responses are likely to be less reliable and will vary between models. Attention has been concentrated on atmospheric dynamics, and we have built up a mechanistic picture of how the seasonal cycle and some annual mean quantities have changed in the GCM. The imposition of fixed sea surface temperatures should be regarded as both an advantage and a limitation. It is a rather restrictive assumption that may have consequences for the phase of the response in the seasonal cycle, particularly since the sea ice edge is constrained by this assumption not to change between the two integrations either. However, even the pure land–atmosphere response shown here has some interesting deviations from simple minded expectations, and it is important to separate these from the effects of poorly known SST variations. The simplicity of this approach will provide a valuable reference point when interpreting results from future integrations in which the ocean is treated interactively.

Apart from the straightforward goal of understanding how a GCM responds to a given change in forcing, it is also of great value to be able to compare the results with geological data. Detailed analysis of GCMs provides the link between the known orbital perturbation and the evidence from the geological record. In this respect, the model has had a remarkable degree of success in reproducing many of the observed signals from around the world. The model has been successful in providing a way in which to view changes such as the summer warming of the Northern Hemisphere continents, the increased Sahel rainfall, the dryness of California and wetness of midwestern United States, and the dryness of northern Europe and wetness of the Mediterranean. On the other hand, there are still some discrepancies between model and data that require explanation, such as the January temperature over eastern Canada and the moisture budget over Australia. A variety of processes has been discussed with respect to each of these phenomena. We have emphasized the importance of large-scale circulation features such as jet streams, transient activity, and deep convection, as well as the divergent monsoon-type circulations appealed to frequently in previous work. This approach has been feasible due to relatively high resolution in a long integration with a full seasonal cycle.

It will be very interesting to compare this work with other, similar GCM integrations within the PMIP pro-

ject. It will also be of great value to investigate individual mechanisms in greater detail and it is hoped that more specific diagnostic projects will follow from this work.

Acknowledgments. We would like to thank Sylvie Jousaume and Karl Taylor for helpful discussions and for providing the standard PMIP parameters for the run. We also thank Mike Blackburn and the two reviewers for their comments on the manuscript. This work was funded by the U.K. Natural Environment Research Council.

REFERENCES

Alexander, R. C., and R. L. Mobley, 1976: Monthly average sea surface temperatures and ice pack limits on a 1° global grid. *Mon. Wea. Rev.,* **104,** 143–148.

Bartlein, P. J., and T. Webb, 1985: Mean July temperature at 6000 years BP in eastern North America: Regional equations for estimates from fossil pollen data. *Quat. Res.,* **22,** 361–374.

Berger, A. L., 1978: Long term variations of daily insolation and quaternary climatic changes. *J. Atmos. Sci.,* **35,** 2362–2367.

Betts, A. K., and M. J. Miller, 1986: A new convective adjustment scheme. Part 1: Observational and theoretical basis. *Quart. J. Roy. Meteor. Soc.,* **112,** 677–691.

COHMAP Members, 1988: Climatic change of the last 18 000 years: Observations and model simulations. *Science,* **241,** 1043–1052.

Gallimore, R. G., and J. E. Kutzbach, 1989: Effects of soil moisture on the sensitivity of a climate model to Earth orbital forcing at 9000 years BP. *Climate Change,* **14,** 175–205.

Hall, N. M. J., B. J. Hoskins, P. J. Valdes, and C. A. Senior, 1994: Storm tracks in a high resolution GCM with doubled carbon dioxide. *Quart. J. Roy. Meteor. Soc.,* **120,** 1209–1230.

Harrison, S. P., and J. Dodson, 1993: Climates of Australia and New Guinea since 18 000 yr B.P. *Global Climates since the Last Glacial Maximum,* H.E. Wright et. al., Eds., University of Minnesota Press, 265–293.

Hoskins, B. J., and P. J. Valdes, 1990: On the existence of storm tracks. *J. Atmos. Sci.,* **47,** 1854–1864.

——, H. H. Hsu, I. N. James, M. Masutani, P. D. Sardeshmukh, and G. H. White, 1989: Diagnostics of the global atmospheric circulation. WCRP Rep. 27, World Meteorological Organization, Geneva, 217 pp. [Available from CGAM, Dept. of Meteorology, University of Reading, U.K.]

Huntley, B., and I. C. Prentice, 1988: July temperatures in Europe from pollen data, 6000 years before present. *Science,* **241,** 687–690.

Klimanov, V. A., 1984: Paleoclimatic reconstructions based on the information statistical method. *Late Quaternary Environments of the Soviet Union,* H. E. Wright Jr. and C. W. Barnosky, Eds., University of Minnesota Press.

Koerner, R. M., and D. A. Fisher, 1990: A record of Holocene summer climate from a Canadian high Arctic ice core. *Nature,* **343,** 630–631.

Kutzbach, J. E., and F. A. Street-Perrott, 1985: Milankovitch forcing of fluctuations in the level of tropical lakes from 18 to 0 kyr B.P. *Nature,* **317,** 130–134.

——, and P. J. Guetter, 1986: The influence of changing orbital parameters and surface boundary conditions on climate simulations for the past 18 000 years. *J. Atmos. Sci.,* **43,** 1726–1759.

——, and R. G. Gallimore, 1988: Sensitivity of a coupled atmosphere/mixed layer ocean model to changes in orbital forcing at 9000 years B.P. *J. Geophys. Res.,* **93,** 803–821.

Liao, X., F. A. Street-Perrott, and J. F. B. Mitchell, 1994: GCM experiments with different cloud parameterizations: Comparisons with paleoclimatic reconstructions for 6000 years B.P. *Paleoclimates—Data and Modelling,* **1,** 99–123.

Markgraf, V., 1993: Climatic history of Central and South America since 18 000 yr B.P.: Comparison of pollen records and model simulations. *Global Climates since the Last Glacial Maximum,* H. E. Wright et al., Eds., University of Minnesota Press, 357–385.

McGlone, M. S., M. J. Salinger, and N. T. Moar, 1993: Paleovegetation studies of New Zealand's climate since the last glacial maximum. *Global Climates since the Last Glacial Maximum,* H. E. Wright et al., Eds., University of Minnesota Press, 294–317.

Mitchell, J. F. B., N. S. Graheme, and K. L. Needham, 1988: Climate simulations for 9000 years before present: Seasonal variations and effect of the Laurentide ice sheet. *J. Geophys. Res.,* **93,** 8283–8303.

Morcrette, J.-J., 1990: Impact of changes to radiative transfer parameterizations plus cloud optical properties in the ECMWF model. *Mon. Wea. Rev.,* **118,** 847–873.

Morley, J. J., and B. A. Dworetzky, 1993: Holocene temperature patterns in the South Atlantic, Southern and Pacific oceans. *Global Climates since the Last Glacial Maximum,* H. E. Wright et al., Eds., University of Minnesota Press, 125–135.

Palmer, T. N., G. J. Shutts, and R. Swinbank, 1986: Alleviation of a systematic westerly bias in general circulation and numerical weather prediction models through an orographic gravity wave parameterization. *Quart. J. Roy. Meteor. Soc.,* **112,** 1001–1040.

Ritchie, J. C., and S. P. Harrison, 1993: Vegetation, lake levels and climate in Western Canada during the Holocene. *Global Climates since the Last Glacial Maximum,* H. E. Wright et al., Eds., University of Minnesota Press, 401–414.

Roberts, N., and H. E. Wright Jr., 1993: Vegetational, lake level and climatic history of the Near East and Southwest Asia. *Global Climates since the Last Glacial Maximum,* H. E. Wright et al., Eds., University of Minnesota Press, 194–220.

Ruddiman, W. F., and A. C. Mix, 1993: The North and equatorial Atlantic at 9000 and 6000 years B.P. *Global Climates since the Last Glacial Maximum,* H. E. Wright, et al., Eds., University of Minnesota Press, 94–124.

Slingo, J. M., 1987: The development and verification of a cloud prediction scheme for the ECMWF model. *Quart. J. Roy. Meteor. Soc.,* **113,** 899–927.

——, M. Blackburn, A. Betts, R. Brugge, K. Hodges, B. Hoskins, M. Miller, L. Steenman-Clark, and J. Thuburn, 1994: Mean climate and transience in the tropics of the UGAMP GCM: Sensitivity to convective parameterization. *Quart. J. Roy. Meteor. Soc.,* **120,** 881–922.

Street-Perrott, A. F., and S. P. Harrison, 1985: Lake levels and climate reconstruction. *Paleoclimate Analysis and Modelling,* A. D. Hecht, Ed., John Wiley, 291–340.

——, and R. A. Perrott, 1993: Holocene vegetation, lake levels and the climate of Africa. *Global Climates since the Last Glacial Maximum,* H. E. Wright et al., Eds., University of Minnesota Press, 318–356.

Thuburn, J., 1993: Use of a flux limited scheme for vertical advection in a GCM. *Quart. J. Roy. Meteor. Soc.,* **119,** 469–487.

Watson, R. T., H. Rodhe, H. Oeschger, and U. Siegenthaler, 1990: Greenhouse gases and aerosols. *Climate Change, The IPCC Scientific Assessment,* J. T. Houghton, G. J. Jenkins, and J. J. Ephraums, Eds., Cambridge University Press, 1–40.

Webb, T., P. J. Bartlein, S. P. Harrison, and K. H. Anderson, 1993: Vegetation, lake levels and climate in eastern North America for the past 18 000 years. *Global Climates since the Last Glacial Maximum,* H. E. Wright et al., Eds., University of Minnesota Press, 415–467.

Winkler, M. G. and P. K. Wang, 1993: The late quaternary vegetation and climate of China. *Global Climates since the Last Glacial Maximum,* H. E. Wright et al., Eds., University of Minnesota Press, 221–264.

Wright, H. E., Jr., J. E. Kutzbach, T. Webb III, W. F. Ruddiman, F. A. Street-Perrott, and P. J. Bartlein, 1993: *Global Climates since the Last Glacial Maximum.* University of Minnesota Press, 569 pp.